



Eddy-driven effects on solute transport in porous media

Zhongxia Li^{1,3}, Xianshuo Yang¹, Shuai Yuan⁴, Junwei Wan¹, Yun Yang⁵, Haibo Feng^{2,3}, Xixian Kang¹, Kun Huang¹, and Chong Ma⁶

¹School of Environmental Studies, China University of Geosciences, 430074 Wuhan, China

²School of Geography and Information Engineering, China University of Geosciences, 430074 Wuhan, China

³Key Laboratory of Mine Ecological Effects and Systematic Restoration, Ministry of Natural Resources, Beijing, 100081, China

⁴The First Geological Brigade of Hubei Geological Bureau, 435000, Huangshi, China

⁵Huaneng Lancang River Hydropower Inc., 650206, Kunming, China

⁶School of Mathematics and Physics, China University of Geosciences, 430074 Wuhan, China

Correspondence: Haibo Feng (haibo_feng@cug.edu.cn)

Received: 17 December 2025 – Discussion started: 2 February 2026

Accepted: 14 April 2026 – Published: 4 May 2026

Abstract. Groundwater pollution poses a significant threat to water resource sustainability. However, while the hydrodynamic impact of pore-scale eddies has been investigated, their quantitative linkage to upscaled macroscopic solute transport parameters remains insufficiently established. This study investigates the effects of hydrodynamic conditions (flow velocity) and porous media structural parameters (particle size, arrangement) on eddy development and solute transport through laboratory experiments and numerical simulations. A novel three-dimensional (3D) quantitative method for characterizing eddy zones was proposed, revealing the mechanisms of eddy formation and their impact on solute breakthrough curves (BTCs). Results indicate that higher flow velocities and larger particle sizes amplify eddy proportions, leading to pronounced BTC tailing due to delayed solute exchange between main flow stream and eddy zones. The mobile-immobile model (MIM) parameters, particularly the immobile zone ratio ($1 - \beta$), showed strong alignment with eddy proportions, reducing inversion ambiguity. Smaller particle sizes diminished early solute breakthrough, while random-packed (RP) media exhibited the slowest solute penetration compared to structured arrangements (SC, FCC, BCC). The study establishes exponential relationships between dilution index and eddy-dominated solute heterogeneity, highlighting structural controls on diffusion coefficients. These findings enhance theoretical frameworks for groundwater solute transport and provide practical

insights for optimizing pollution remediation strategies in porous media systems.

1 Introduction

Effective prevention and control of groundwater pollution is a global priority, yet remediation remains challenging due to the inherent complexity of aquifer systems (Burri et al., 2019; Llamas and Martínez-Santos, 2005; Shah et al., 2003). Most quantitative assessments of groundwater transport rely on the macro-scale seepage assumption, which simplifies actual pore-space movement into a linear velocity field through solid particles (Harr, 2012). However, this simplification often overlooks the complex curved motion and boundary-driven eddies that occur at the pore scale, which significantly govern flow resistance and solute distribution (Lee and Babadagli, 2021; Li et al., 2023; Polubarinova-Kochina et al., 2015; Vaughan, 2009; Wang, 2004).

While traditional advection-diffusion models assume Fickian behavior, a growing body of evidence shows that breakthrough curves (BTCs) in porous media frequently exhibit non-Fickian characteristics, such as early arrival and significant tailing (Brusseu et al., 1989; de Vries et al., 2017; Šimunek et al., 2006; Tang et al., 1981). This behavior is largely attributed to the heterogeneous distribution of flow velocities and the trapping of solute in stagnant or recircu-

lating zones, known as eddies (Dou et al., 2019; Zheng et al., 2022), which dramatically increase residence times and complicate remediation efforts.

It is noteworthy that eddy formation can be driven by inertial effects rather than exclusively by fully developed turbulence. Within this context, the flow conditions investigated in this study, characterized by Reynolds numbers ranging from 113 to 1697, fall within the laminar to transitional regime where such inertial effects dominate. The complexity of pore structures determines that eddies are one of the most common and easily occurring phenomena in actual groundwater flow, significantly influencing the distribution of flow velocity and the migration of substances. While advanced observational techniques have been developed to tackle pore-scale dynamics, they face significant constraints. Methods such as micro-Particle Image Velocimetry (micro-PIV) are highly effective in microfluidic applications but strictly require transparent media and refractive index matching, limiting their use in 3D opaque packings. Conversely, non-destructive 3D imaging techniques, including dynamic X-ray Micro-CT and Magnetic Resonance Velocimetry (MRV), provide excellent structural resolution but often struggle with the temporal resolution and field-of-view required to capture rapid, transient recirculating flows in larger macroscopic columns. Because directly quantifying the dynamic 3D eddy volume solely through physical experiments remains technologically prohibitive, there is a critical need for coupled approaches. This study bridges this gap by combining physical solute transport experiments with rigorously validated 3D numerical simulations, allowing for the precise extraction of internal eddy structures that physical sensors cannot capture.

Although the impact of complex boundary morphology on pore-scale flow fields is well-documented, bridging this hydrodynamic understanding to predict solute transport presents a formidable scientific challenge. Tracking the dynamic, three-dimensional mass exchange between high-velocity advective channels and low-velocity recirculating eddies requires mapping localized concentration gradients across microscopic fluid boundaries. Experimentally capturing these real-time, micro-scale diffusion processes demands exceedingly high spatiotemporal resolution, rendering them largely invisible to traditional macroscopic column studies that only measure bulk effluent. Furthermore, computationally coupling non-linear fluid dynamics with solute transport at resolutions fine enough to resolve internal eddy mass-transfer is highly demanding. Consequently, the explicit mechanisms by which these transient hydrodynamic structures dictate macroscopic non-Fickian tailing have remained an unresolved gap in the literature. By employing high-fidelity, three-dimensional coupled models alongside physical experiments, this study aims to directly penetrate this “black box” and quantify the eddy-driven solute exchange process.

The currently mobile-immobile model (MIM) is often used to describe the non-Fickian transport behavior observed

in solute transport within porous media affected by eddies (Gouze et al., 2008; Hasan et al., 2019; Karadimitriou et al., 2016). The MIM model divides the water flow into two parts: the mobile zone and the immobile zone. The solute exchange between the different regions occurs through molecular diffusion, and the exchange intensity depends on the concentration difference in different regions (Gao et al., 2010; Kohne et al., 2004). The parameters related to the MIM model, such as the proportion of the immobile zone, can only be retrieved by fitting the BTCs. Additionally, the uncertainty of the MIM model is increased because the physical meaning of relevant parameters cannot be clearly defined during the calibration process, which limits the range of parameter values.

To further explore the generation, development, and evolution of eddies, as well as their influence on solute transport processes under different hydrodynamic conditions (different velocities) and the main controlling factors of porous media structure (different particle sizes and arrangement), this study designed various types of porous media models and conducted a series of laboratorial physical model experiments and numerical simulations. Firstly, a new quantitative characterization method of three-dimensional (3D) eddy area proportion is proposed. Secondly, the mechanism of different flow velocities, particle sizes and arrangement patterns on the formation, development and evolution of eddies and their influence on solute transport was revealed from the 3D pore scale. Finally, the relationship between the parameters of the MIM model and the structural parameters of the porous medium is quantified, which can provide scientific support for the prevention and control of groundwater pollution, and enrich the basic theories of groundwater seepage and solute transport.

2 Materials and methods

2.1 Model design and experimental apparatus

To investigate the mechanisms by which the structure of different types of porous media affects the development and evolution of eddies, this study designed four different types of porous media, including simple cubic (SC), face-centered cubic (FCC), body-centered cubic (BCC), and randomly packed (RP). The SC is the loosest pore structure, and the arrangement is gradually tight from FCC to BCC, and the corresponding porosity is 0.476, 0.398, and 0.266, respectively. The randomly packed porosity is 0.645. Subsequently, we can determine the coordinates of each sphere once they achieve mechanical equilibrium. The geometric model of the randomly packed porous media is constructed by integrating MATLAB. It is worth mentioning that the particle sizes of pore media in different arrangement modes are consistent, and a total of 5, 8, 10, 15 mm different particle sizes are designed. The different types of porous media models are shown in Fig. 1.

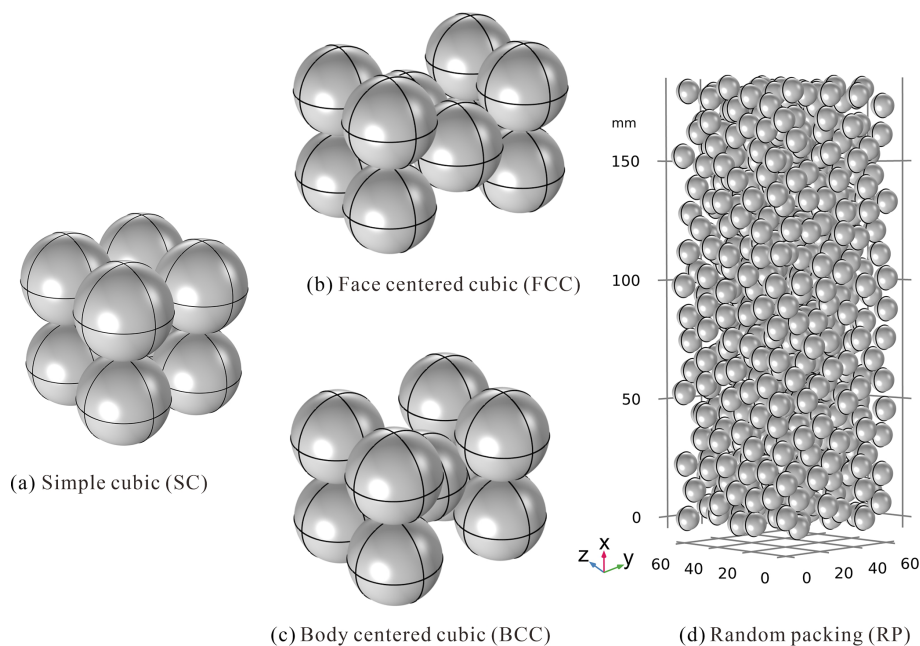


Figure 1. Diagram of different types of porous media models.

Considering the limitations of traditional physical model experiments, we choose the SC packed model to carry out laboratory seepage and solute transport experiments. According to our previous research (Huang et al., 2013), we found that the wall effect (the flow resistance caused by the tube wall) could be disregarded when the number of spheres in the cross-section of the experimental tubes reached 6×6 . The schematic diagram and physical diagram of the experimental device are shown in Fig. 2.

The tracer delivery system and imaging system were added on the basis of the seepage experimental device. The experimental tube section is composed of three parts: the inlet and outlet transition section and the porous media section. The total length of the experimental tube section is 150 cm, the pellet filling section is 100 cm, and the length of the inlet and outlet transition section is 25 cm. The transition section is designed to mitigate the effects of inlet and outlet influences. Additionally, a dissipative plate with numerous small holes is installed at the inlet transition section to ensure a more stable flow of water entering the system. The medium section is filled with artificially bonded cubic spheres arranged in a specific pattern, and pressure measurement ports are located 5 cm away from both the inlet and outlet. The measurement system consists of three components: flow, pressure, and temperature measuring devices. The flow rate after stabilization is calculated using the volumetric method. By monitoring the pressure changes between the two pressure measurement ports using a pressure sensor, a quantitative relationship between seepage resistance and flow velocity can be obtained.

To investigate the effects of different influencing factors (such as different flow velocities, particle sizes, and arrangement) on the solute transport process, the selected tracer should not react with the porous media and should have low adsorption properties. Due to its stable chemical properties and good visibility, Brilliant Blue was chosen as the tracer for this solute transport experiment. The photography method involves capturing images or videos of Brilliant Blue concentrations at different time intervals using high-resolution camera (FDR-AX60, SONY). The quantitative relationship between solute concentration and image information can be established by obtaining information from images of a fixed concentration of Brilliant Blue solution (such as grayscale values or RGB values), allowing for the determination of solute concentrations at different times. Compared to the sampling method, the photography method does not disturb the flow field and is easy to operate, which has been widely used. To address the concern regarding light source variation, we implemented a strict protocol: the light source, camera, and column positions were fixed, and each image was corrected using a reference image taken with pure water under identical conditions. Most importantly, the calibration curve was developed under the exact same lighting settings as the experiments, meaning the concentration-grayscale relationship inherently accounts for the specific illumination field, ensuring robust relative measurements. The relationship between the concentration of Brilliant Blue and the grayscale values of the photographs we obtained is shown in Fig. 3, displaying a clear negative power-exponential relationship. Strictly speaking, the observation concerning the increased uncer-

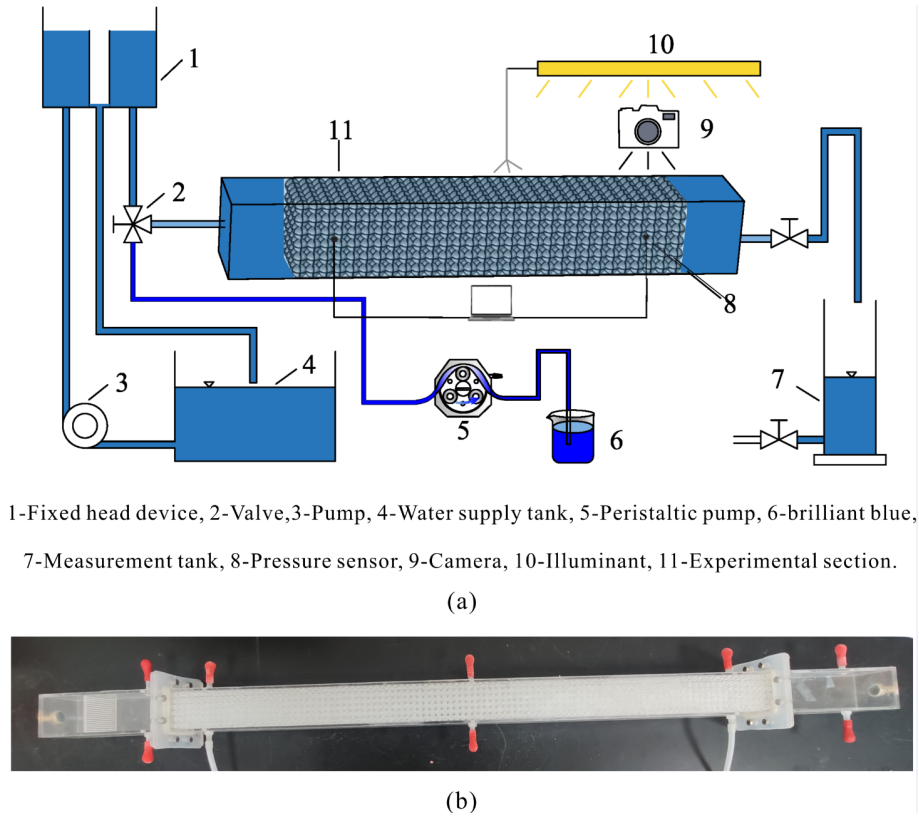


Figure 2. Schematic diagram of solute transport experimental setup.

tainty in low-concentration estimation from the calibration curve, which is an inherent limitation of the optical method.

2.2 Numerical simulation methods and model validation

It is very difficult or almost impossible to obtain the 3D seepage field of porous media by traditional physical model experiment. With the rapid development of computational fluid dynamics, numerical simulation has been widely used in the study of groundwater seepage (Banaei et al., 2021; Yang et al., 2019; Yu et al., 2023), which also has a good effect on the simulation of porous media using COMSOL Multiphysics® (Banaei et al., 2021; Koohbor et al., 2023). The COMSOL Multiphysics® is a finite element method-based fluid simulation software that can simulate fluid flow in porous media by solving the conservation equations and the Navier-Stokes equations for incompressible fluids. The transport process of solute in porous media was simulated using the advection-diffusion equation coupled with the flow field. And the governing equations are shown as follows:

$$\rho \nabla \cdot \mathbf{u} = 0 \tag{1}$$

$$\rho (\mathbf{u} \cdot \nabla) \mathbf{u} = \mu \nabla^2 \mathbf{u} - \nabla p \tag{2}$$

$$\frac{\partial C}{\partial t} + \nabla \cdot \mathbf{J} + \mathbf{u} \cdot \nabla C = 0 \tag{3}$$

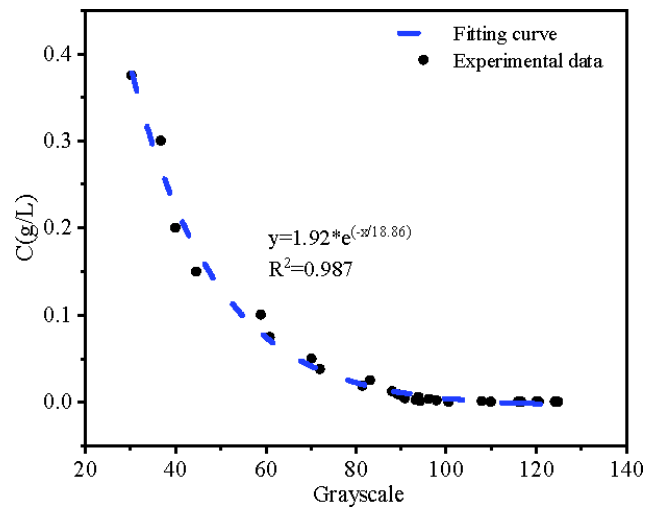


Figure 3. A quantitative relationship between brilliant blue concentration and grayscale image.

$$\mathbf{J} = -D\nabla C \quad (4)$$

where ρ is the fluid density, ∇ is the gradient operator, \mathbf{u} is the velocity vector in 3D coordinate system, μ is the dynamic viscosity, and p is the total pressure. As for the solute field, C is the injection concentration of the solute, \mathbf{J} is the mass flux diffusive flux vector, D is the diffusion coefficient.

Experiments and corresponding numerical simulations were conducted on the SC model under different flow velocities. It is essential to ensure that the dimensions of the numerical model are fully consistent with those of the experimental section. The inlet boundary is set as a velocity boundary, the outlet boundary is set as a pressure boundary, and the model wall is set as a no-slip boundary with zero flow. Besides, the density of water is 998.2 kg m^{-3} , and the dynamic viscosity is $1 \times 10^{-3} \text{ Pa} \cdot \text{s}$. The concentration at the inlet boundary is set to 0.079 g L^{-1} , the right side of the model is set as the outflow boundary, and the wall is set as a zero-flux boundary. The molecular diffusion coefficient of the solute is set to $2 \times 10^{-9} \text{ m}^2 \text{ s}^{-1}$. Then, the corresponding flow field and solute field are obtained by controlling different inlet velocities. The preprocessing of the model has a significant impact on the results of numerical simulations. The overall accuracy of the model mesh generation is controlled by setting the boundary layer and the number of grid elements. On the one hand, the selected mesh size should not be too large, otherwise it will not be able to reflect the real model structure, on the other hand, the mesh size should not be too small, which will consume much more computer resources, and the calculation results cannot even converge. The COMSOL Multiphysics® can offer nine levels of grid sizes, and an independent mesh convergence analysis was conducted (as shown in Fig. 4). The results demonstrate that the selected fine-level grid, coupled with boundary layer refinement, ensures grid-independent solutions, accurately resolves near-wall velocity gradients, and optimally balances computational efficiency. In our previous research, The COMSOL Multiphysics® was also applied to the simulation of the seepage field and solute field in rough conduit media, achieving good results (Li et al., 2024).

To ensure the accuracy of the simulated flow field, we validated the numerical hydraulic gradient against the experimental v – J data detailed in our previous work (Huang et al., 2013). Because the current experimental apparatus is directly built upon this previously validated seepage device and uses identical SC packings, its baseline hydrodynamic behavior is strictly represented by this established dataset, providing a rigorous foundation for the subsequent solute transport modeling. We have compared the numerical simulation results with the experimental results, and the relationship between hydraulic gradient (J) and specific discharge (v) in porous media with SC packing is plotted in Fig. 5a. To avoid confusion, we should point that \mathbf{J} indeed represents the mass diffusive flux vector, which is a vector quantity (bold in italics).

Conversely, in Fig. 5a, J was used to denote the hydraulic gradient, a scalar quantity.

We can see that the hydraulic gradient in the simulation results is slightly less than that in the experimental results; even so, the simulation results fit well with the experimental results overall. When the particle size of spheres remains the same, the hydraulic gradient increases with the increasing specific discharge. While the specific discharge is somewhere the same, a smaller particle size leads to a greater hydraulic gradient. In other words, the smaller particle size needs to overcome the stronger seepage resistance. Notably, the fitting error between the experimental and simulated hydraulic gradients for the $D = 5 \text{ mm}$ case is slightly higher than that of the larger particle cases (e.g., $D = 8 \text{ mm}$ and $D = 10 \text{ mm}$). This is likely due to the increased influence of the column wall effect and local structural heterogeneity inherent in smaller particle packings. In these tighter configurations, the ratio of the wall-zone porosity to the bulk porosity creates more significant preferential flow paths, posing a greater challenge for the idealized 3D numerical model to perfectly capture the experimental bulk seepage resistance. In this study, the experimental hydraulic data (v – J curves in Fig. 5a) provided the primary validation for the flow field. Since Brilliant Blue is an inert tracer, its transport is predominantly advection-diffusion under the studied conditions. Therefore, accurately replicating the flow field is the most critical factor for reliable solute transport simulations. The strong agreement between experimental and simulated v – J relationships demonstrates the accuracy of the flow field, thereby validating the foundation for the subsequent solute transport results. To explicitly validate the solute transport model, we compared the simulated breakthrough curves at the column outlet with the experimental BTCs obtained via the photographic tracer method under representative flow conditions, which is plotted in Fig. 5b.

The numerical model successfully captures the macroscopic non-Fickian transport features observed in the physical experiment. Specifically, the simulation accurately reproduces both the early arrival of the solute front and the pronounced late-time tailing. This direct agreement confirms that the coupled advection-diffusion model, built upon the validated flow field, reliably simulates the mass exchange processes between the main flow channels and the eddy zones, thereby providing a robust foundation for the subsequent pore-scale analysis.

2.3 Identification of eddy zone in 3D scale

Due to the complexity of porous media structure, the streamlines are obstructed during the seepage process, resulting in the formation of numerous eddy zones. However, it is very difficult to directly extract the volume of eddy area in 3D porous media. Different methods for identifying the eddy area in 3D scale was proposed based on the definition of zero flux in eddy zones (Zhou et al., 2019) and the velocity prob-

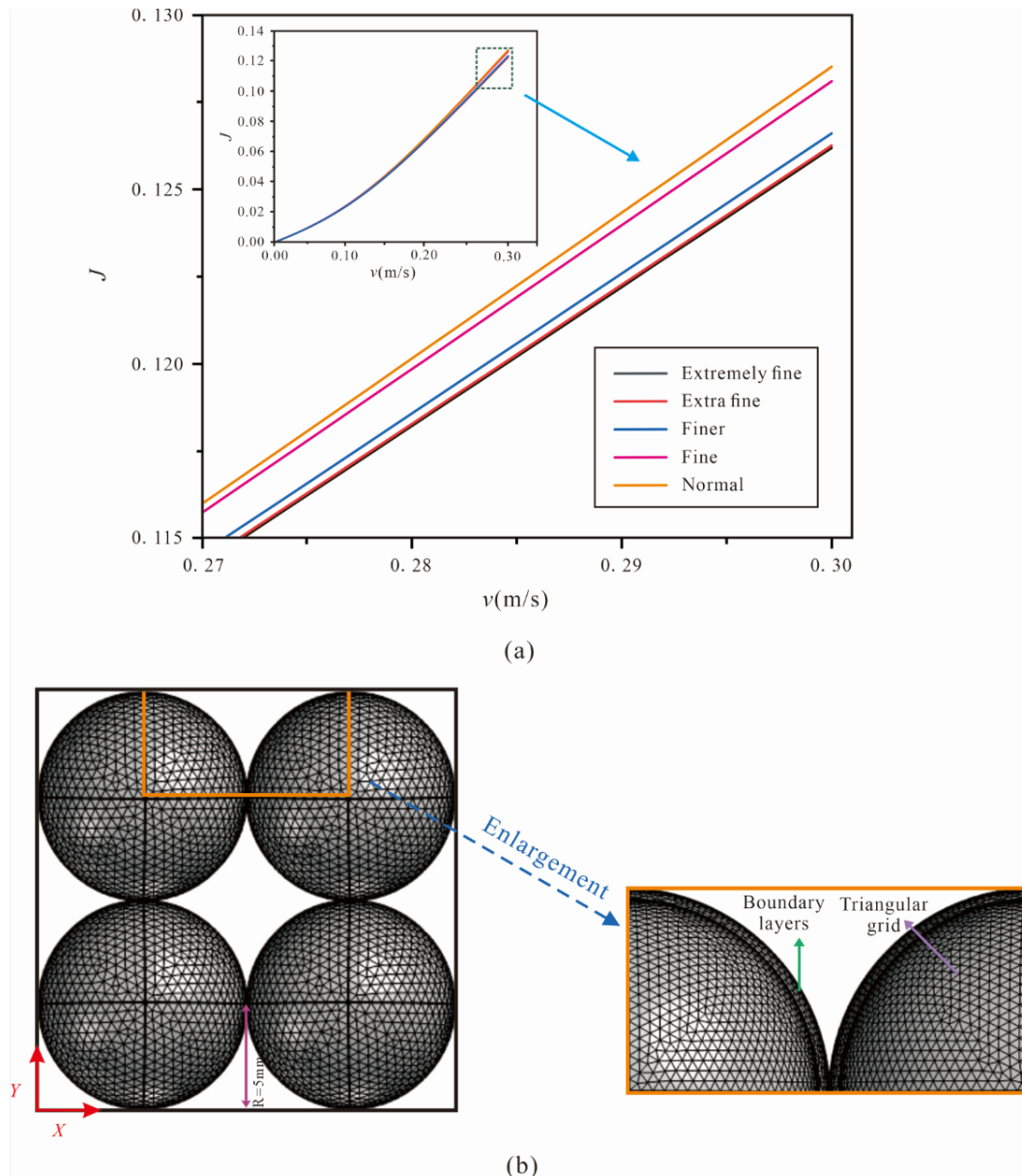


Figure 4. Mesh independence analysis and local boundary layer mesh details. **(a)** Grid convergence curves showing the relationship between hydraulic gradient (J) and specific discharge (v) under different mesh densities. **(b)** Visualization of the local mesh distribution and boundary layer refinement around the spherical particles ($D = 5$ mm).

ability density function (PDF), see details in Bijeljic et al. (2013).

Taking the SC model as an example, firstly, we sliced the 3D porous media model using the xz plane (with the x -axis as the flow direction). Multiple cross-sections are set along the y -axis to ensure that the number of slices can effectively cover the entire model, as shown in Fig. 6a, and further export the velocity field data of different 2D sections. We can see that the colors at different positions are different, reflecting different flow velocities through the local magnification of the 2D slice flow field, as shown in Fig. 6b. The flow ve-

locity is lower in the areas where eddies are generated, while the flow velocity at the main flow stream is relatively large. To analyze the flow velocity characteristics of the eddy area and their impact on solute transport, we further obtained the flow velocity and concentration data at different times along the white section line (which includes the main flow stream and the eddy area, see Fig. 6b) according to the numerical simulation results, as shown in Fig. 6c. It can be seen from Fig. 6c that the flow velocity curve exhibits three peak velocity segments and two low velocity segments. Combined with Fig. 6b, we can see that the region with high velocity corre-

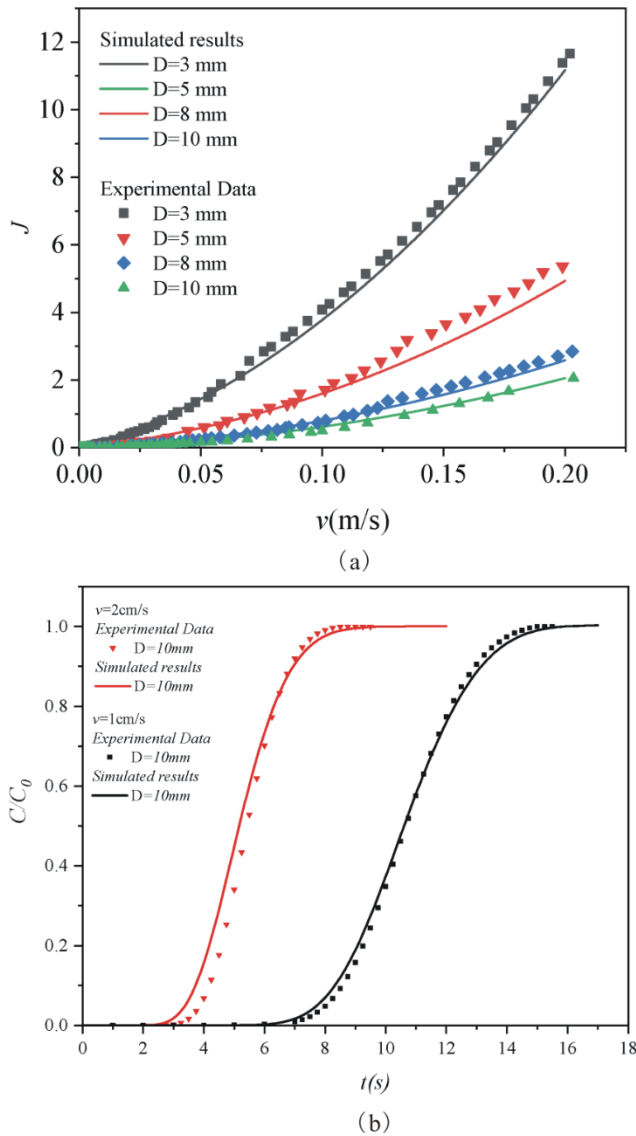


Figure 5. (a) Comparison of experimental and numerical simulated J – v curves for SC packed porous media. (b) Comparison of experimental and numerical simulated breakthrough curves (BTCs) under representative flow velocities ($v = 1 \text{ cm s}^{-1}$ and $v = 2 \text{ cm s}^{-1}$) for the SC packed porous media with a particle size of $D = 10 \text{ mm}$.

sponds to the main flow stream, while the region with low velocity corresponds to the eddy area. The flow velocity of the main flow stream is significantly higher than that of the eddy area, approximately 20 times the velocity in the eddy area. Moreover, we can clearly observe that there is a significant point of mutation in the flow velocity between the main flow stream and the eddy zone (the blue curve in Fig. 6c). In addition, we selected two arbitrary moments (t_1 , t_2) during the solute attenuation process to obtain the solute concentrations in both the main flow stream and the eddy zone. It can be observed that the solute concentrations in the eddy zone are significantly higher than those in the main flow stream.

This is due to the relatively low flow velocity in the eddy zone, along with the bending and deflection of streamlines, which allows the solute to be captured by eddies, slowing down the diffusion process into the main flow stream.

To compare the velocity differences at various positions within the flow field, we performed normalization using the average flow velocity (v_{av}), which is actually the inlet flow velocity. We classify the velocities at different positions in 3D space and obtained the velocity probability density function (PDF) and cumulative probability density function (CDF) under different inlet flow velocities, allowing us to compare the changes in the proportion of low-velocity areas under different flow velocity conditions. Based on the velocity difference between the main flow stream and the eddy zone, we can obtain the critical flow velocity (v_c), which is the significant point of mutation mentioned above. The process of using the PDF and CDF to quantify the eddy area in a 2D slice, which is then integrated to obtain the 3D proportion, is indeed a key aspect of our analysis, which divided into five steps: Firstly, using the self-developed MATLAB code to process the acquired 2D seepage field data. For a given 2D slice (e.g., an xz plane at a specific y -coordinate, as in Fig. 6a), we export the velocity magnitude at every grid point within the fluid domain. We then calculate the PDF and CDF of these velocity values for that specific slice. The horizontal axis of this plot is the velocity normalized by the average inlet velocity (v/v_{av}). As shown in Fig. 6c, we identify a critical flow velocity (v_c) that represents the inflection point separating the low velocities in the eddy zones from the high velocities in the main flow channels. The value of the CDF corresponding to this normalized critical velocity (v_c/v_{av}) directly gives the area fraction of that specific 2D slice where the velocity is less than or equal to v_c . This area fraction is our quantitative measure of the “eddy area” for that slice. By repeating this PDF/CDF analysis for a dense series of parallel 2D slices spanning the entire model (along the y -axis), we obtain the eddy area fraction for each slice. The eddy area proportion for the entire 3D model is then calculated by integrating (averaging) these 2D area fractions across all slices. This method provides a robust and objective way to quantify the complex 3D eddy volume from 2D slice data. Furthermore, while the v_c threshold identification via the PDF or CDF inflection point was established here for relatively uniform packings, its statistical nature suggests potential robustness for heterogeneous natural media. Although a wider particle size distribution would broaden the velocity PDF, the physical transition between advective channels and recirculating zones (eddy) should still manifest as a characteristic inflection in the CDF. This provides a physically-grounded and consistent basis for eddy quantification across diverse and complex porous structures, even where pore-scale geometry is highly irregular.

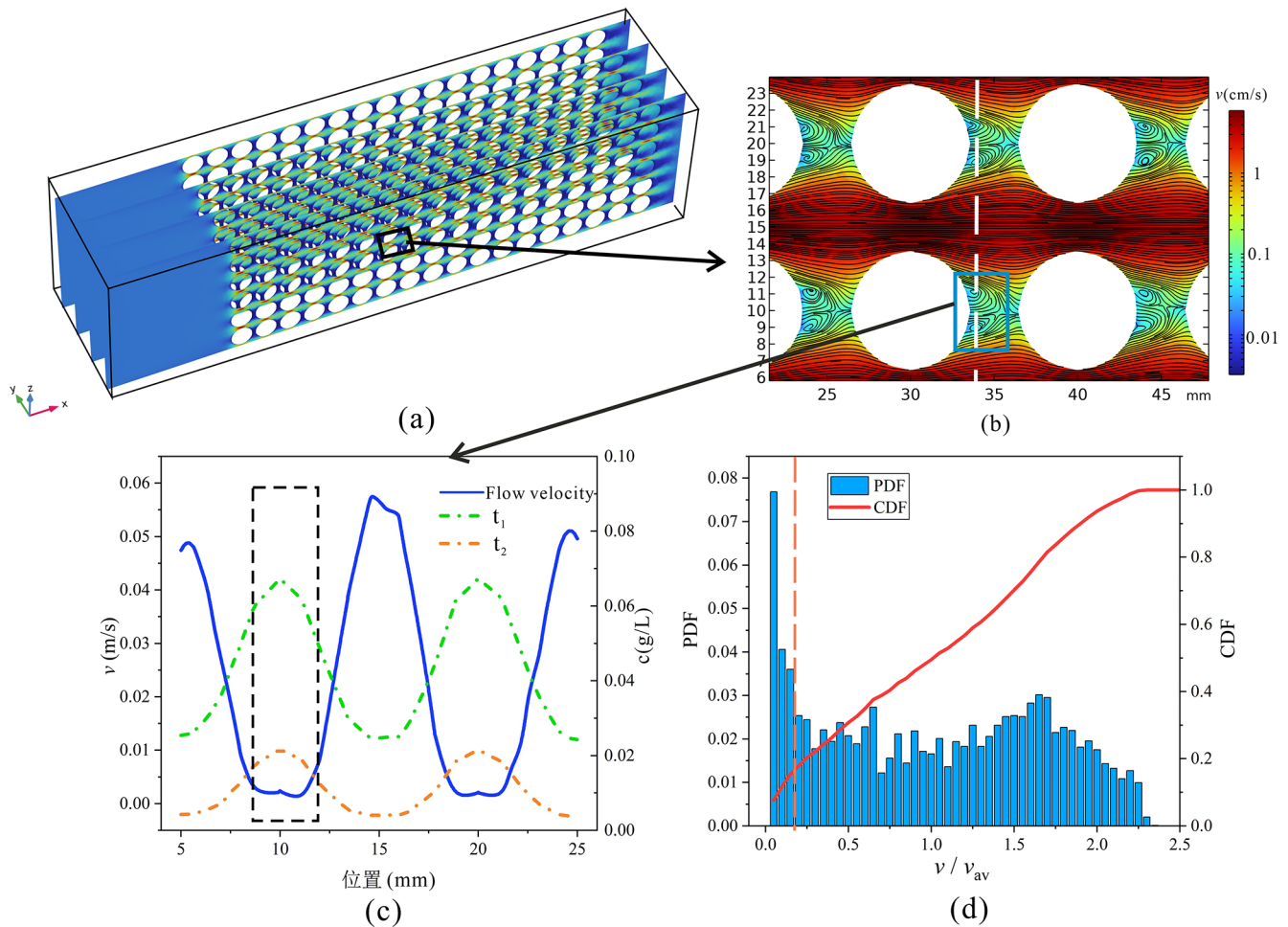


Figure 6. Schematic diagram of eddy extraction in porous media.

3 Results and discussion

3.1 Effects of different flow velocities on solute transport

We selected the SC model with a particle size of 10 mm to conduct numerical simulations at four different flow velocities (including 0.5, 1, 1.5, and 2 cm s^{-1}), and the 2D slice flow fields are shown in Fig. 7. The Reynolds numbers ($Re = \rho v_{\text{pore}} d_p / \mu$) range from 113 to 1697, where the average pore velocity (v_{pore}) is used as the characteristic velocity and the particle diameter (d_p) as the characteristic length scale. This range encompasses all experimental conditions, providing a standardized metric to characterize the flow. We have chosen to maintain our analysis based on direct flow velocity for the specific objectives of this study. Our focus is on establishing a direct, intuitive link between the hydrodynamic driving force (velocity) and the resulting eddy development and solute transport behavior. The red areas indicate the main flow stream with high velocity, while the blue ar-

reas represent the low-velocity regions formed in the porous medium structure.

We can see from Fig. 7 that the flow velocity in the main flow stream is significantly greater than that in the eddy area. When the flow velocity is 0.5 cm s^{-1} , the streamlines are deflected due to obstructions, leading to the formation of eddies; however, the eddy area proportion is quite small. With the continuous increase of flow velocity, we can obviously see that the eddy proportion increases significantly. This aligns with our previous research conclusions that the eddy proportion will ultimately approach a theoretical maximum value (Xiong et al., 2024). When the flow state developed to a fully stable condition, we continuously injected the brilliant blue and conducted solute transport experiments in SC model porous media with particle sizes of 5 and 10 mm, using five flow velocities of 0.2, 0.5, 1, 1.5, and 2 cm s^{-1} . The BTCs under different flow velocities are obtained, as shown in Fig. 8, where the horizontal coordinate was logarithmic and the vertical coordinate normalized the concentration (C/C_0). And the corresponding dilution concentration

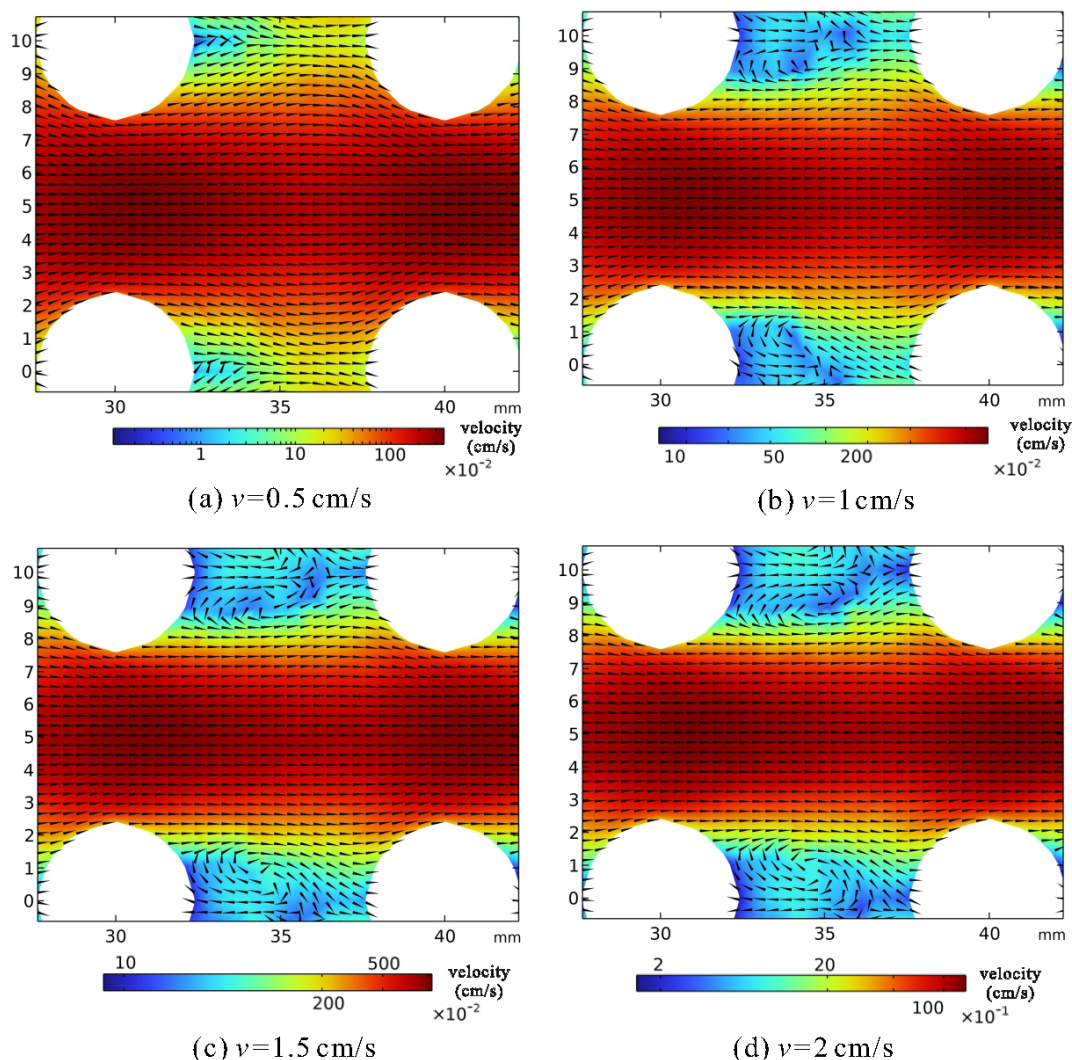


Figure 7. The 2D slice flow fields of the SC model with a particle size of 10 mm at different flow velocities.

under different inlet flow velocities is defined as the respective initial concentration (C_0).

We can see from Fig. 8 that the BTCs for both particle sizes shift to the left as the flow velocity increases, indicating that the penetration time decreases. The residence time of water within the pore space increases at lower flow velocities. This longer contact time allows for a more complete solute equilibration via diffusion between the main flow and the larger, more developed eddy zones present at lower velocities. Consequently, a greater mass of solute is stored in the eddies, which is then released slowly, causing the pronounced tailing. At higher velocities, the reduced contact time and different eddy dynamics limit this equilibration process, leading to less tailing. This correction accurately reflects the interplay between advection timescales and diffusive exchange. Although the tailing of the BTCs is a consistent and robust physical observation, the definitive quantitative analysis of concentrations at very low values

($C/C_0 < 0.05$) is constrained by the increasing uncertainty of the optical calibration method at these levels. Therefore, the specific values in the late-time tail should be interpreted with appropriate consideration of this methodological limitation. To further quantify the eddy effect at different flow velocities and their impact on the characteristics of the BTCs, we established a quantitative relationship between the times corresponding to the BTC concentrations reaching 5% and 98% of the input solute concentration (t_5 and t_{98}) (Hou et al., 2018) and the different flow velocities, respectively, as shown in Fig. 9.

It can be seen from Fig. 9 that t_5 and t_{98} show a power-law decreasing relationship with the flow velocity, indicating that eddy effect has a significant influence on the penetration process of solute. With the flow velocity increases, the eddy area proportion continues to increase, while the proportion of the main flow stream decreases. The increase in flow velocity within the main flow stream results in the solute arriving

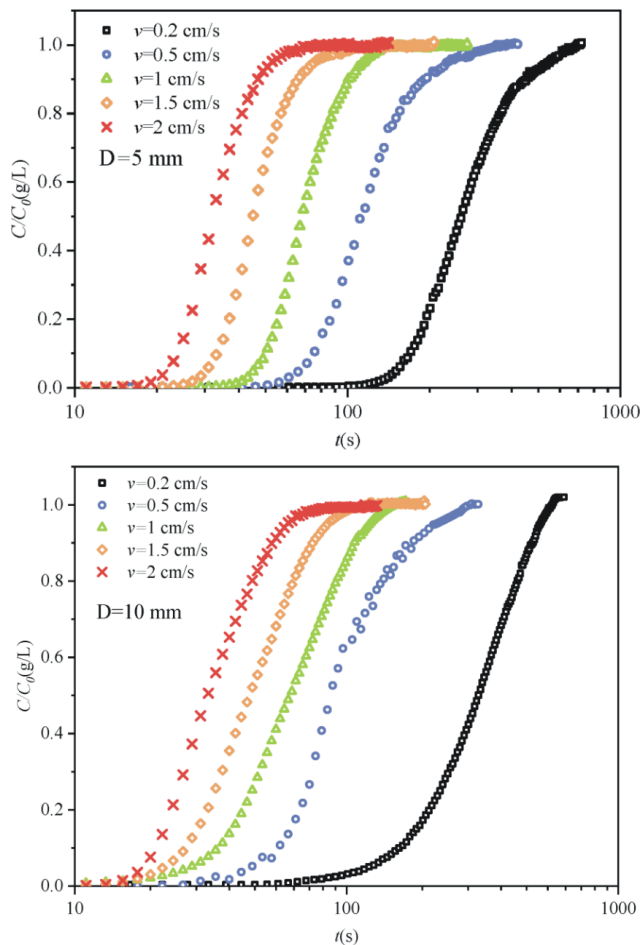


Figure 8. The BTCs of SC model porous media with 5 and 10 mm particle sizes at different flow velocities.

earlier. Additionally, it can be observed that the reduction of t_{98} is significantly greater than that of t_5 . Taking the porous medium with a particle size of 5 mm as an example, when the flow velocity increases from 0.2 to 2 cm s⁻¹, the value of t_5 decreases by approximately 130 s, while the value of t_{98} decreases by about 450 s, indicating that the changes of flow velocity have a more pronounced effect on the tailing process of the BTCs.

3.2 Effects of different particle sizes on solute transport

The SC model porous media consisting of four different particle sizes (including 5, 8, 10, 15 mm) was selected for related numerical simulations. The inlet flow velocity is controlled at a constant 2 cm s⁻¹, and the 2D slice flow field is shown in Fig. 10. In this study, for a given packing arrangement (e.g., Simple Cubic – SC), the porosity remains constant regardless of the particle size. This is a fundamental characteristic of regular, ordered packings; the porosity is determined solely by the geometric arrangement of the spheres. Therefore, when we investigate the effect of particle size (e.g., 5,

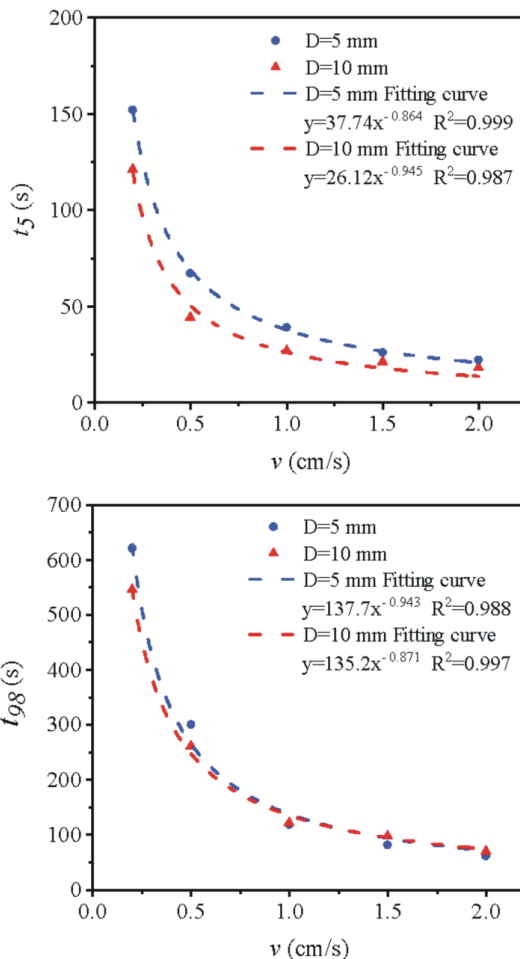


Figure 9. The relationship between characteristic times (t_5 and t_{98}) of BTCs and different velocities with different particle sizes.

8, 10, 15 mm spheres in an SC packing), we are specifically isolating the effect of scaling the pore geometry (i.e., the absolute size of the pores and throats) while the porosity, a measure of the pore volume fraction, is held constant. This allows us to independently analyze the impact of the particle size on eddy development and solute transport.

To facilitate the comparison of flow fields between different particle sizes, we adjusted the scale to ensure that the different particle sizes appear consistent. Then, it is easier to visually compare the velocity differences between the low-speed eddy area and the high-speed main flow stream. In Fig. 10, the blue area represents the low-velocity eddy area, while the red area indicates the high-velocity main flow stream. Besides, we can observe that when the flow velocity remains constant, the larger particle size led to the larger eddy area and larger rotational velocity inside the eddy area. To explore the impact of different eddy developments on solute transport, we obtained the BTCs under various particle size conditions after injecting the solute, as shown in Fig. 11.

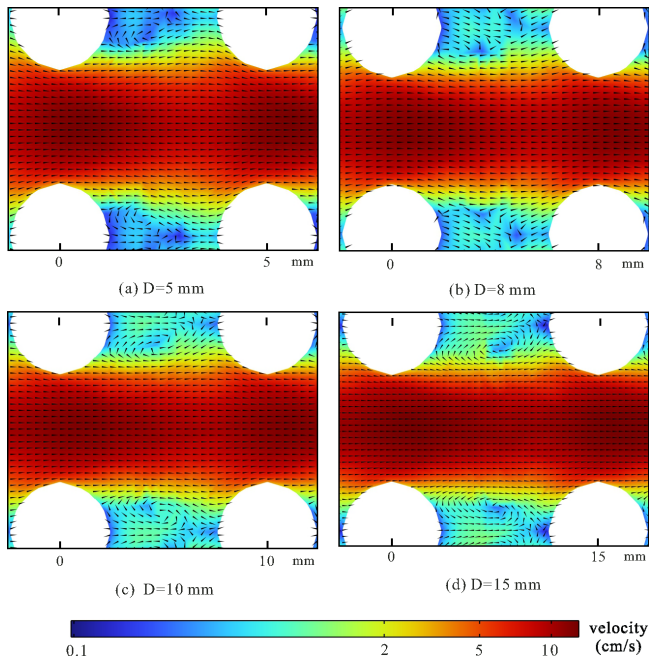


Figure 10. Schematic diagram of the flow field of SC model porous media with different particle sizes ($v = 2 \text{ cm s}^{-1}$).

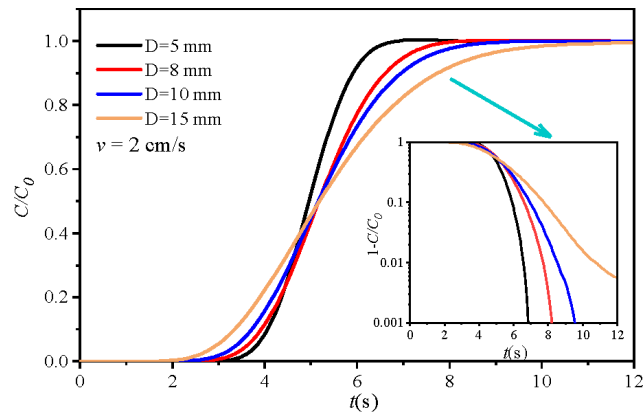


Figure 11. The BTCs of SC model porous media with different particle sizes.

We found that the BTCs of different particle sizes show significant differences, exhibiting anomalous early arrival times under the same flow velocity conditions. The BTCs of the porous media with a particle size of 15 mm shows the earliest breakthrough, while the solute penetration in the porous medium with a particle diameter of 5 mm the slowest. Furthermore, as the particle size decreases, there is a diminishing trend in the early breakthrough phenomenon of the solute, which is consistent with the above results of flow fields with different particle sizes (eddy development). In the process of solute transport in porous media, the rapid flow in the main flow stream significantly influences the early arrival of the BTCs. To more intuitively observe the morphology of so-

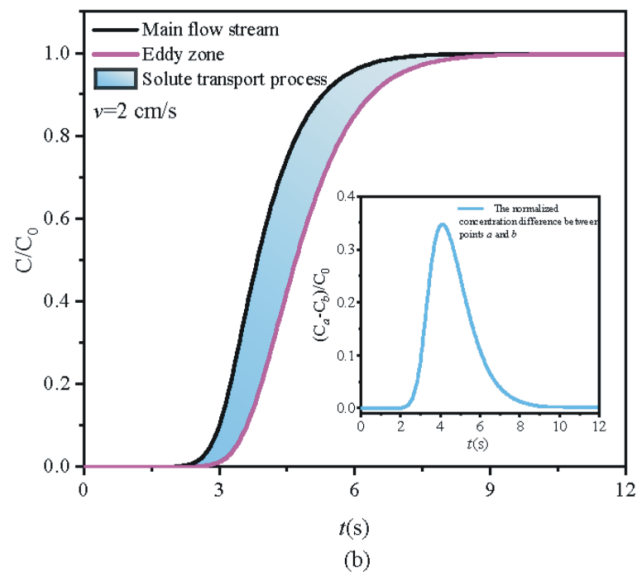
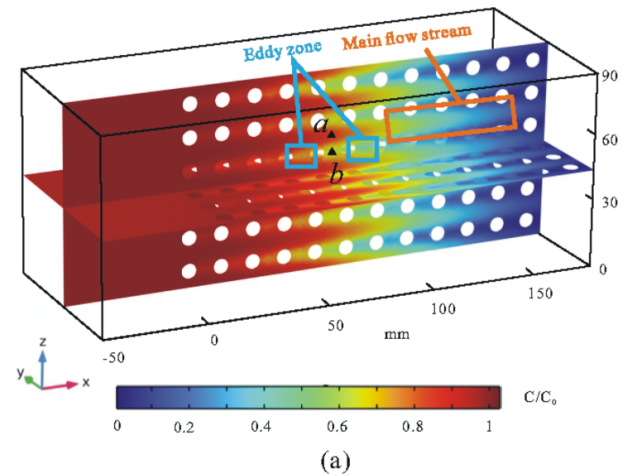


Figure 12. (a) The solute field distribution of SC model porous media ($t = 5 \text{ s}$, $D = 15 \text{ mm}$, D is particle size). (b) The comparison of the BTCs between the main flow stream and the eddy area.

lute peak, we selected a porous media model with a particle size of 15 mm as an example and obtained the solute distribution at 5 s after solute injection, as shown in Fig. 12a. In addition, we selected two characteristic points (points *a* and *b* in Fig. 12a) in the main flow stream and the eddy area, respectively, and obtained their BTCs, as shown in Fig. 12b.

We can see that due to the rapid flow in the main flow channels, multiple distinct solute peak leading edges have been observed. The concentration of solute in the eddy area is significantly lower than that in the main flow stream, and the concentration of solute in the eddy area shows an obvious lag compared with that in the main flow stream. We selected the feature points *a* and *b* of the main flow stream and eddy area respectively, and obtained their normalized concentration curves over time, as shown in Fig. 12b. It can be observed that due to the lag in the eddy area, the solute con-

centration in the main flow stream is always greater than that in the eddy area. The shaded blue area in Fig. 12b represents the process of solute transfer between the main flow stream and the eddy area caused by the concentration difference between the two points. We further magnified this process and plotted the normalized concentration difference between the main flow stream and the eddy area (the feature points *a* and *b*). The concentration peaked at 4.1 s, showing a trend of initially increasing and then decreasing, and exhibiting a trailing asymmetry, which indicating that the mass transfer rate between the main flow stream and the eddy area slows down.

To quantify the impact of eddy effect on the degree of heterogeneous distribution of solute under different particle size conditions, the dilution index proposed by Kitanidis (1994) was used to characterize the dilution state of solute plumes during solute transport. The value of the dilution index represents the volume of the solute plume within the pore volume of the porous media. For continuous injection scenarios, the value of the dilution index closer to 1 indicates a higher ratio of the solute plume occupying the entire pore volume of the media. Once the solute is injected into the porous media, due to the inhomogeneity of the medium structure and flow field, the value of the normalized dilution index will gradually increase. Then, the normalized dilution index can reflect the inhomogeneity of the solute distribution in the porous media. Besides, Dou et al. (2018) evaluated the impact of eddy effect on the uneven distribution of solutes in fractured media using the dilution index. The equation for the solute dilution index $E(t)$ in 3D porous media is as follows:

$$E(t) = \exp \left[- \int_V p(x, y, z, t) \ln(p(x, y, z, t)) dV \right] \quad (5)$$

$$p(x, y, z, t) = \frac{c(x, y, z, t)}{\int_V c(x, y, z, t) dV} \quad (6)$$

where $p(x, y, z, t)$ is the distribution function of the mass. In this study, the normalized dilution index was used to quantify the influence of eddy effect on the uneven distribution of solute in porous media with different particle sizes. When the flow velocity is 2 cm s^{-1} , the relationship between the normalized dilution index of porous media and the dimensionless time parameter t' (the pore volume) with different particle sizes was shown in Fig. 13. The t' represents the time process of solute transport, and the equation is as followed:

$$t' = \frac{Qt}{Al} \quad (7)$$

where Q is the flow flux at the outlet, t is the time of solute transport, and Al is the volume of the pore.

We can see from Fig. 13 that the normalized dilution index varies with the dimensionless time parameter in three stages: Firstly, when $t' < 0.12$, the normalized dilution index increases slowly; when $0.12 < t' < 1$, the normalized dilution index increases sharply; and while $t' > 1$, the normalized dilution index remains almost stable, respectively. In the initial

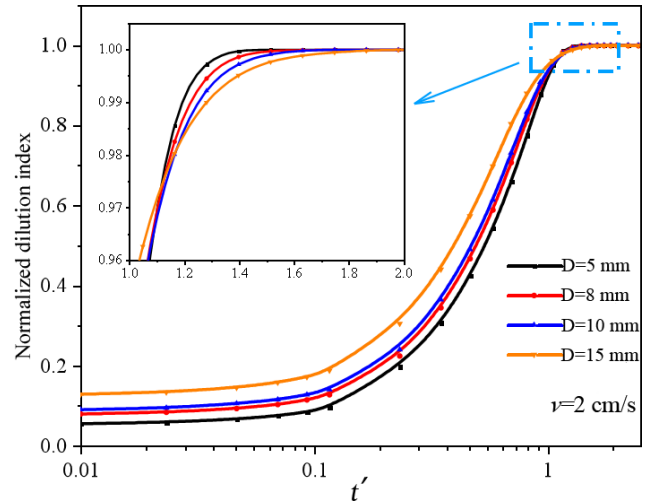


Figure 13. The relationship between the normalized dilution index and the dimensionless time parameter (SC models).

stage of solute entering the porous media, the solute preferentially transfers in the main flow stream, while the transfer to the eddy area is still relatively low. Then, the solute transport between the main channel and the eddy area gradually increases. In the later stage of solute transport, the retention of the solute by the eddy area results in a pronounced tailing effect during the penetration process. In addition, we found that larger particle sizes lead to larger normalized dilution index when $t' < 1$, which is related to the pore structure formed by the SC models with different particle sizes and the development of the eddies. For porous media with larger particle size, the larger volume of a single pore leads to a larger volume of eddy area, resulting in a higher degree of inhomogeneity of the solute distribution. When $t' > 1$, a completely opposite trend is observed.

As we know, larger particle sizes lead to a higher eddy proportion and greater initial flow heterogeneity. However, the larger individual pore bodies in these media also host larger, more coherent eddy structures. While these large eddies initially trap solute and create a highly uneven distribution (low normalized dilution index for $t' < 1$), they also provide a larger volume for diffusive mixing to act upon over time. The mass transfer between the main channel and these sizable eddy zones is governed by diffusion across longer characteristic paths, making it a slower process. Consequently, the system with larger grains requires a longer time to achieve a homogeneous state. After the primary advective pulse has passed ($t' > 1$), this slower, more complete back-diffusion from the large, well-developed eddies eventually leads to a higher degree of homogeneity (a higher normalized dilution index) compared to systems with smaller grains, where the pore structure is more confined and complex, potentially limiting the final extent of mixing. This interpretation, consistent with the mechanisms discussed in studies like Dou et al.

(2018), highlights the time-dependent competition between heterogeneity-driven trapping and volume-enhanced diffusive mixing.

In this study, we employed the dimensional dimensionless time parameter t' (e.g., Fig. 13) strategically. Using actual time as the x -axis in several figures (e.g., Figs. 8 and 11) was intentional, as it allows for a more intuitive understanding of the temporal scale of the observed non-Fickian transport phenomena, such as the absolute time of early arrival and the duration of tailing. This provides a direct, physical sense of the retardation caused by eddies. Meanwhile, the use of dimensionless time in other figures facilitates the comparison of the shape of the BTCs independent of the system's specific volume. We believe this dual approach offers complementary insights.

3.3 Effects of different arrangement patterns on solute transport

Different arrangement modes have significant influence on the structure of porous media. This section will describe in detail the eddy evolution of porous media with different arrangement modes (including SC, FCC, BCC and RP), when the inlet flow velocity is 2 cm s^{-1} , the obtained flow field is shown in Fig. 14.

We can see from Fig. 14 that the flow fields of porous media with different arrangement modes are completely different, and different colors respectively represent the main flow stream with high flow velocity (red area) and the eddy area with low flow velocity (blue area). Due to the relatively regular structure of the porous medium in SC model, the pore abdomen can provide a larger development space for eddies, so the volume of the eddy area formed by the SC model is larger than that of the other three arrangements. The spatial positions of eddies in porous media with different arrangement modes are also completely different. As for the RP model, we have observed several very interesting phenomena: The structure is further complicated due to the randomness of the arrangement of the spheres. On the one hand, two distinct preferential flow channels are formed; on the other hand, we observed regions with lower flow velocities, called dead-end-pores (Bordoloi et al., 2022). The identified eddy zones are not stagnant regions but are characterized by active recirculation. As evidenced by the velocity profile in Fig. 6c, the flow velocity within these zones, while significantly lower than in the main flow channels, is distinctly non-zero. This observation is consistent with the findings of Bordoloi et al. (2022), who emphasized that laminar vortices enhance dispersion through their inherent rotational motion. The quantification of these dynamic eddy zones forms the basis for analyzing their role in solute mass transfer and the emergence of non-Fickian transport behavior.

Besides, we also agree that porosity is a fundamental property that profoundly influences flow and transport. We recognize that porosity is not an independent variable here but is a

direct consequence of the packing geometry. The substantial difference in porosity (e.g., almost 2 times between SC and BCC) is an inherent and defining characteristic of these distinct arrangements. Therefore, the analysis in Sect. 3.4 inherently addresses the combined effect of the specific pore structure and the resulting porosity. Discussing porosity as a separate, parallel factor to arrangement would create a mismatch in the logical hierarchy of influencing factors, as porosity is an emergent property of the arrangement. Our approach was to treat “arrangement” as a holistic factor that encapsulates both the geometric configuration and the resultant porosity. We believe this provides a more integrated understanding of how systematic changes in the medium's architecture control eddy development and solute transport.

To understand the influence of different arrangement patterns forming eddies on solute transport, we obtained the solute distribution characteristics in various porous media at 3 s after injection, as shown in Fig. 15.

We can see from Fig. 15 that different types of porous media models all present relatively obvious preferential flow channels, although they differ from each other. The Fig. 15a show that the preferential flow channel formed are parallel to each other due to the good connectivity of the pore abdomen in the SC model. The Fig. 15b and c indicate that the difference in solute distribution between the FCC and BCC porous media is primarily manifested in the eddies caused by different pore structures. Compared to the FCC model, an additional sphere present in the pore abdomen of the BCC model occupy more pore space, resulting in a lower eddy proportion, which causes the solute peak in the BCC model to appear more uniform. The Fig. 15d shows that the RP porous media structure is more chaotic, leading to a more uneven solute front with multiple preferential flow paths. Additionally, we further obtained the BTCs of porous media with different arrangements at a flow velocity of 2 cm s^{-1} , especially detailing the solute penetration process at different times in the RP model of porous media, as shown in Fig. 16.

We can see from Fig. 16a that the characteristics of the BTCs of porous media models with different arrangements are completely different when the flow velocity remains consistent. The penetration process of the BCC model is the fastest, followed by the FCC and SC models, while the penetration process of the RP model is the slowest. Among different types of porous media models, the RP model has the highest porosity, followed by the FCC model, while the BCC model has the lowest porosity, which indicate that the structure has a significant impact on the solute penetration process. To compare the effect of eddies on the tail of the BTC, the $1 - C/C_0$ logarithmic coordinate plot is used to process the BTCs (see Fig. 16a). We noticed that the BTCs of the SC model and the RP model are nearly overlapping at the tail, and the higher eddy area proportion lead to the greater impact on the trailing effect. It is worth noting that the numerical results, including the low-concentration tails down to relative concentrations of 0.001, are not significantly affected by nu-

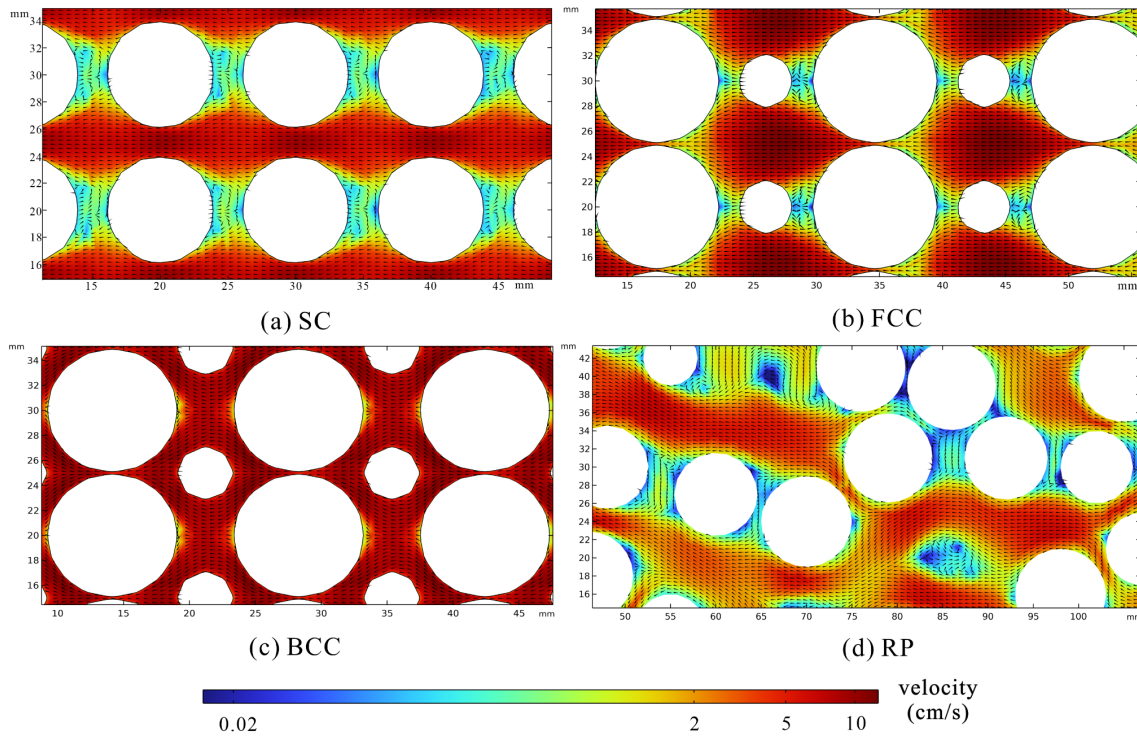


Figure 14. Schematic diagram of flow field and eddy area of porous media with different arrangement modes ($v = 2 \text{ cm s}^{-1}$).

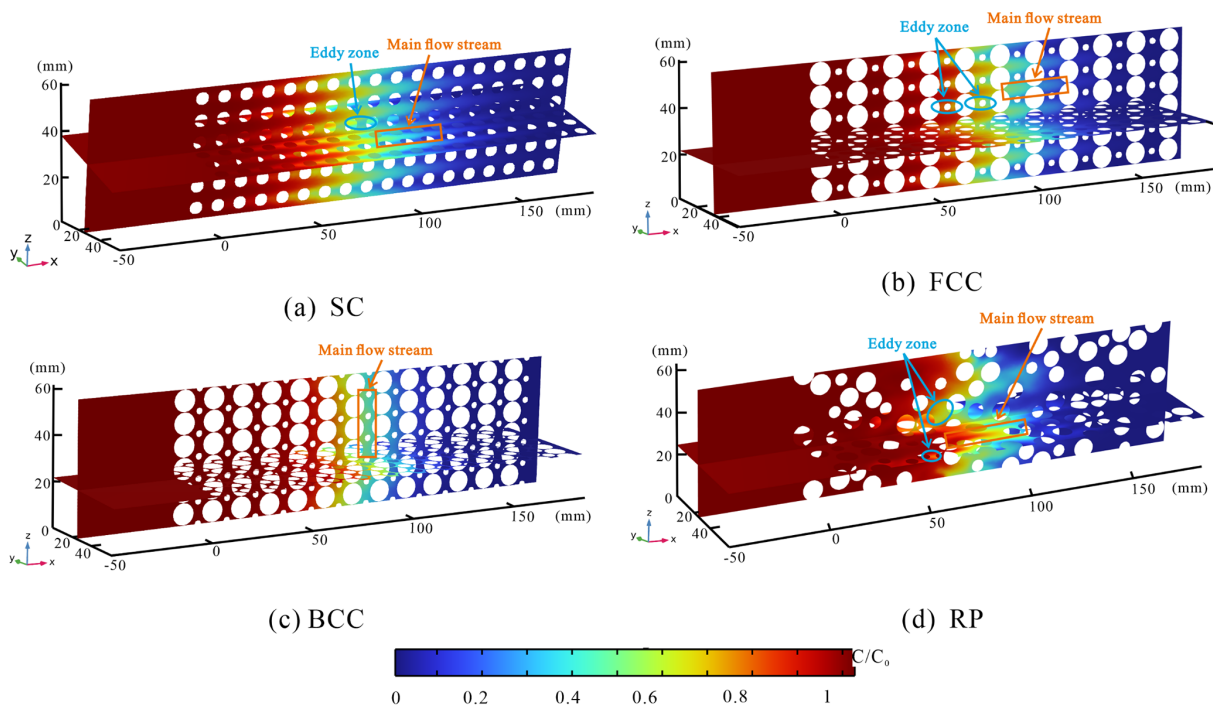


Figure 15. Solute distribution in porous media with different arrangement patterns.

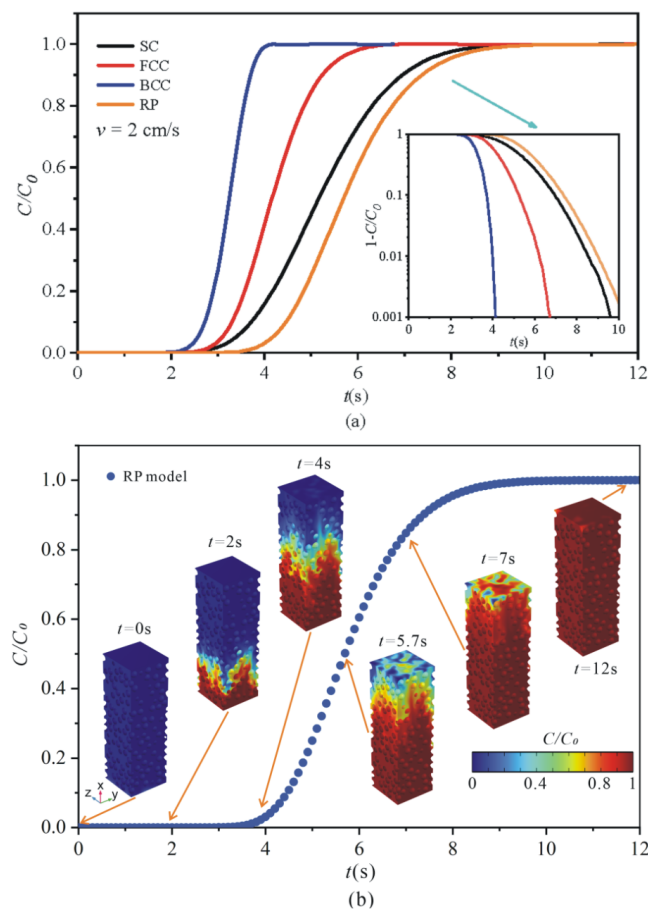


Figure 16. (a) The BTCs of different types of porous media with flow velocity of 2 cm s^{-1} . (b) The RP model penetration process at different times ($v = 2 \text{ cm s}^{-1}$).

merical dispersion. The observed tailing in the BTCs (e.g., Fig. 16a) is a physical phenomenon resulting from mass exchange between the mobile zone and the eddy (immobile) zones, not a numerical artifact, thereby confirming the reliability of our conclusions regarding tailing behavior.

Specifically, the first arrival time (t_5) and the late-stage tailing time (t_{98}) are extracted from the BTCs for each arrangement (SC, FCC, BCC, RP). These metrics provide a direct quantitative measure of the “early arrival” and “tailing” phenomena, respectively. The eddy zone proportion and characteristic breakthrough times for different packing arrangements at an average inlet velocity of 2 cm s^{-1} are shown in Table 1.

Table 1 has been added summarizing the eddy zone proportion alongside the corresponding t_5 and t_{98} values for each packing structure. This quantitative data reveals a clear and consistent trend. The eddy zone proportion, which is a direct consequence of the pore structure created by the packing arrangement, shows a strong correlation with the characteristic times. The quantitative relationship between packing arrangement, eddy development, and solute transport char-

Table 1. The eddy zone proportion and characteristic breakthrough times for different packing arrangements at an average inlet velocity of 2 cm s^{-1} .

Arrangement	Eddy Zone Proportion	t_5 (s)	t_{98} (s)
SC	0.148	3.35	8.10
FCC	0.061	3.05	5.95
BCC	0.008	2.60	3.95
RP	0.040	4.15	8.55

acteristics is unequivocally demonstrated in Table 1. The results indicate that the pore structure, determined by the specific packing arrangement, exerts a primary control on the proportion of eddy zones. This proportion, in turn, directly governs the key features of non-Fickian transport. A clear positive correlation is observed between the eddy zone proportion and the late-time tailing, quantified by t_{98} . For instance, the SC arrangement, with the highest eddy proportion (0.148), exhibits the most pronounced tailing ($t_{98} = 8.10 \text{ s}$), whereas the BCC structure, with a minimal eddy proportion (0.008), shows the fastest clearance ($t_{98} = 3.95 \text{ s}$). While the early arrival time (t_5) is generally earlier in structures with fewer flow obstructions (e.g., BCC), the significantly delayed arrival in the RP model underscores the additional influence of flow path tortuosity and connectivity, beyond the mere volume of eddy zones.

This quantitative analysis powerfully substantiates our qualitative arguments. It demonstrates unequivocally that the packing arrangement controls solute transport by determining the development of eddies, which in turn quantifiably governs the degree of both early arrival and tailing observed in the BTCs. This provides a robust, data-driven link between medium structure and non-Fickian transport dynamics.

4 Solute transport model

The solute transport model is of significant importance for predicting and quantifying the process of solute migration. The conventional mobile-immobile (MIM) transport model is used to describe the non-Fickian transport behavior such as early arrival and trailing in porous media. Considering the complexity of the porous media structure, the MIM model divides the pores into mobile and immobile regions. The solute mass exchange occurs between the mobile and immobile regions during the migration process controlled by advection–diffusion effect. Due to the low flow velocity characteristics of the immobile region, the process of receiving and releasing solute is very slow, leading to the tailing of the BTC. The MIM model simulates the breakthrough process of solutes in porous media by coupling the solute transfer equations between the mobile and immobile regions within the porous media. For the inert solutes, the governing equations of the

MIM model are as followed without considering the adsorption and degradation.

$$\theta_m \frac{\partial C_m}{\partial t} + \theta_{im} \frac{\partial C_{im}}{\partial t} = \theta_m D_m \frac{\partial^2 C_m}{\partial x^2} - v_m \frac{\partial C_m}{\partial x}$$

$$\frac{\partial C_{im}}{\partial t} = \alpha (C_m - C_{im}) \quad (8)$$

$$\beta = \frac{\theta_m}{\theta_{im} + \theta_m} \quad (9)$$

where θ_{im} is the total immobile zone ratio, θ_m is the total mobile zone ratio, D is the effective longitudinal dispersion coefficient, v_m is the velocity in mobile region, and α is the first-order mass transfer coefficient (which depends on diffusion coefficient and other geometric factors), C_m and C_{im} represent the concentrations of mobile and immobile regions, respectively, β is the proportion of mobile region in porous media. While Brilliant Blue is practically treated as an inert tracer in our physical experiments, it is theoretically possible that very slight, reversible physical sorption onto the artificial spheres could occur. If present, this minor sorption would induce additional solute retardation, potentially compounding the observed non-Fickian tailing. However, a major advantage of incorporating numerical simulations in this study is the ability to perfectly isolate physical heterogeneity. Because our numerical model explicitly defines the solute as strictly non-reactive (controlled solely by advection-diffusion mechanics without sorption terms) and still accurately reproduces the pronounced tailing behavior, we can confidently conclude that the tailing quantified herein is dominantly driven by physical hydrodynamic retention within the eddy zones, rather than chemical sorption.

According to the characteristics of the MIM model, the main flow stream is generalized as the mobile region of the model, and the eddy area is generalized as the immobile region of the model, which show clear physical meaning and provide a basis for parameter inversion of the MIM model. The migration of a pulse solute in porous media can be divided into three different stages: In the initial stage, the concentration of solute in the main flow stream is higher than that in the eddy zone when the solute pulse is first introduced into the porous media, leading to solute migration primarily through advection. During the second stage, as the solute pulse encounters the eddy zone, solute mass transfer occurs due to molecular diffusion, allowing some of the solute mass from the main flow stream to gradually enter the eddies. In the third stage, as the solute pulse moves downstream past the eddy zone, the concentration in the main flow stream decreases rapidly, while the concentration in the eddy zone becomes higher than in the main flow stream. At this point, the solute in the eddy zone diffuses back into the main flow stream, resulting in tailing of the BTCs in the main flow stream.

The effect of eddies on solute storage aligns well with the applicable conditions of the MIM model. The eddy zone

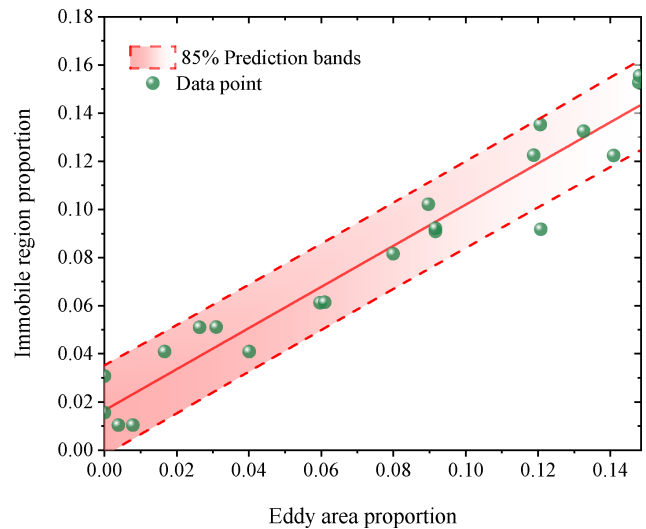


Figure 17. The relationship between the eddy proportion in porous media with the immobile region proportion ($1 - \beta$).

proportion was obtained directly from the flow field simulations using the quantitative 3D characterization method detailed in Sect. 3.1, which is based on a critical velocity threshold derived from the velocity PDF/CDF analysis. Conversely, the immobile zone proportion ($1 - \beta$) was obtained independently by calibrating the MIM model (Eqs. 8 and 9) against the numerical breakthrough curves (BTCs). To validate whether the eddy proportion is consistent with the immobile region proportion ($1 - \beta$) derived from the MIM model, the relationship between the eddy proportion in porous media with varying flow velocities, different particle sizes, and different arrangements was obtained, as shown in Fig. 17.

The abscissa of Fig. 17 represents the eddy area proportion, and the ordinate is the immobile region proportion ($1 - \beta$) derived from the MIM model. If the immobile region proportion cluster around the red line with a slope of 1 passing through the origin in the figure, which indicates that generalizing the eddy zone proportion as the immobile region proportion derived from the MIM model is reasonable. We can see from Fig. 17 that all data points are located on either side of the red line, with almost all of them falling within the 85 % prediction band. The strong correlation observed between these independently obtained parameters validates that the physical eddy zones, identified hydrodynamically, effectively function as the immobile zones in the conceptual MIM model. This provides a physical basis for the MIM parameter and reduces its inversion ambiguity.

However, different flow velocities, particle sizes and arrangements will affect the development of eddies in the porous media, influencing the mass transfer process between the main flow stream and the eddy zone. Therefore, we further discussed the variations of the parameters in the MIM model under different control conditions.

Table 2. The characteristic values of MIM model with different factors.

Average inlet flow velocity (m s ⁻¹)	Particle size (mm)	D_{MIM}	α	RMSE
0.02		$6.00E-04$	0.023	0.0027
0.015		$5.88E-04$	0.009	0.0064
0.01	5	$5.41E-04$	0.004	0.0043
0.005		$4.78E-04$	0.001	0.0154
0.002		$2.73E-04$	0.002	0.0130
0.02		$1.73E-03$	0.018	0.0060
0.015		$1.71E-03$	0.012	0.0096
0.01	10	$1.57E-03$	0.013	0.0150
0.005		$1.07E-03$	0.010	0.0200
0.002		$2.68E-04$	0.005	0.0250
Average inlet flow velocity (m s ⁻¹)	Particle size (mm)	D_{MIM}	α	RMSE
0.01	5	$2.27E-05$	0.277	0.0077
	8	$3.99E-05$	0.269	0.0080
	10	$5.98E-05$	0.282	0.0064
	15	$1.21E-04$	0.303	0.0063
0.02	5	$5.29E-05$	0.494	0.0081
	8	$1.04E-04$	0.492	0.0074
	10	$1.51E-04$	0.490	0.0055
	15	$3.21E-04$	0.531	0.0036
Average inlet flow velocity (m s ⁻¹)	Arrangement	D_{MIM}	α	RMSE
0.01	SC	$5.98E-05$	0.282	0.0064
	FCC	$4.84E-05$	0.230	0.0075
	BCC	$3.37E-05$	0.096	0.0115
	RP	$4.78E-05$	0.110	0.0014
0.02	SC	$1.51E-04$	0.490	0.0055
	FCC	$1.05E-04$	0.250	0.0026
	BCC	$6.55E-05$	0.090	0.0117
	RP	$9.93E-05$	0.120	0.0014

The mass transfer coefficient (α) and the dispersion coefficient (D_{MIM}) are critical parameters in the MIM model. While α quantifies the rate of mass exchange across the interface between the mobile and immobile regions, D_{MIM} physically represents the longitudinal mechanical dispersion within the active flow channels (the mobile region). The results indicate that D_{MIM} increases with the eddy proportion. This trend is attributed to the fact that growing eddies constrict the effective flow pathways, intensifying local velocity gradients and flow tortuosity within the mobile zone, which ultimately enhances the mechanical dispersion process. The mass transfer coefficient and diffusion coefficient under the influence of different control factors are shown in Table 2.

The parameters for the Mobile-Immobile Model (MIM) were determined through an inverse modeling procedure directly within the COMSOL Multiphysics[®] environment. The governing equations of the MIM (Eqs. 8 and 9) were imple-

mented, and the model parameters (including the mass transfer coefficient, the diffusion coefficient in the mobile zone, and the immobile zone ratio) were estimated by coupling the parameter estimation module with a nonlinear least-squares optimization algorithm. This algorithm iteratively adjusted the parameter values to minimize the difference between the simulated breakthrough curves (BTCs) and the concentrations predicted by the MIM, thereby identifying the optimal parameter set that best represents the observed non-Fickian transport behavior for each specific simulation scenario. It should be emphasized that the MIM parameter inversion was performed exclusively on the numerical simulation BTCs rather than the experimental data. This strategy was specifically chosen to bypass the inherent optical measurement uncertainties at low concentrations (as discussed in Sect. 2.1), ensuring that the quantification of the late-time tailing and the derived immobile zone ratio ($1 - \beta$) are robust and un-

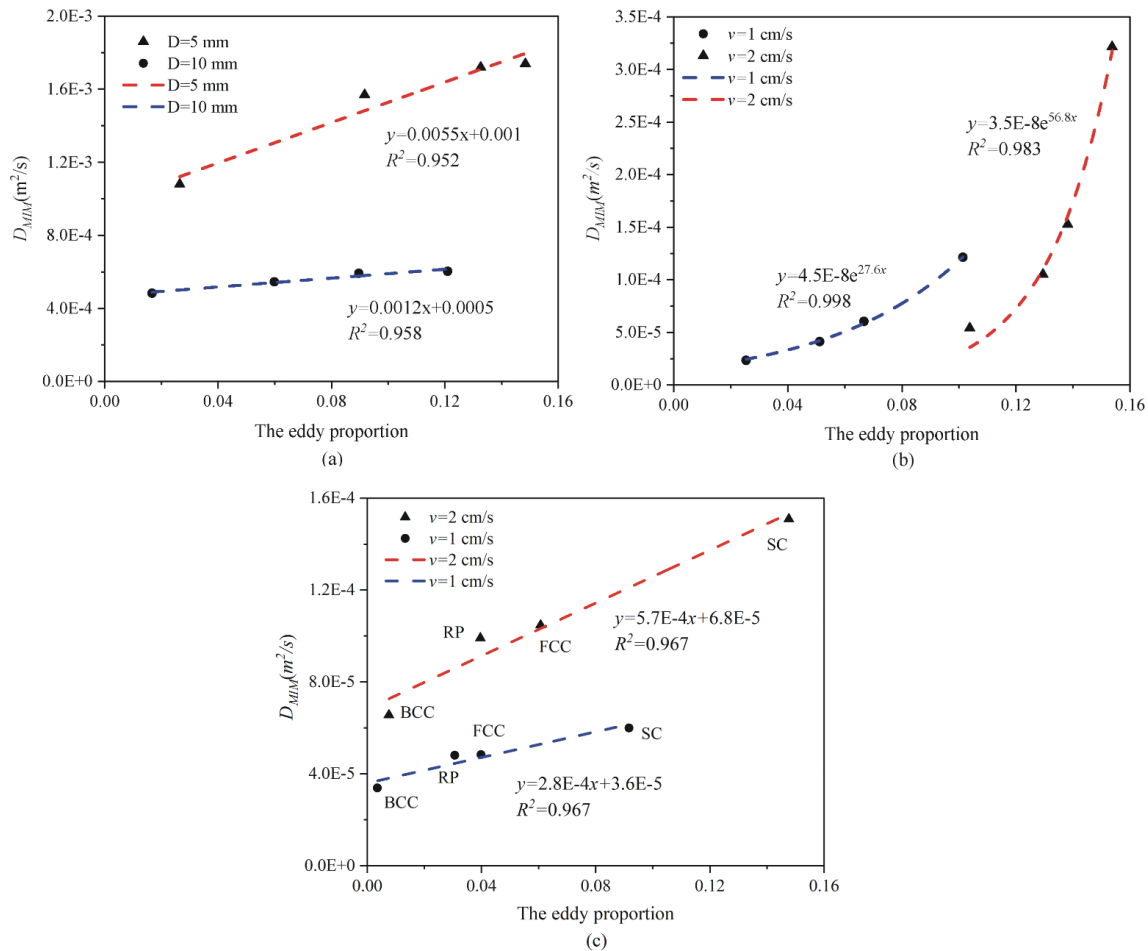


Figure 18. The relationship between the eddy proportion corresponding to the three influencing factors and the diffusion coefficient.

affected by experimental detection limits. To ensure the reliability and uniqueness of the fitted parameters, a sensitivity analysis was conducted, and the root mean square error (RMSE) was calculated for each case, as provided in Table 2. The robustness of the fitted parameters was ensured by verifying the stability of the solution and the convergence of the optimization routine. The mass transfer coefficient and diffusion coefficient increase gradually with the gradual increase of the inlet flow velocity when the particle size remain the same, which is closely related to the development of the eddies. We further obtained the relationship between the eddy proportion corresponding to the three influencing factors and the diffusion coefficient, as shown in Fig. 18, and Fig. 18a and b are both SC arrangements.

It can be seen from Fig. 18a that the diffusion coefficient is positively proportional to the eddy proportion. With the increase of inlet flow velocity, on the one hand, the eddy proportion is increased, on the other hand, the rotational velocity of the eddy zone is also increased, then the solute transport process between the main flow stream and the eddy zone and the solute dispersion in the entire porous media

are accelerated. In addition, the slope of the red fitting line ($D = 10$ mm) in Fig. 18a is larger than that of the blue fitting line ($D = 5$ mm), which also indicates that the influence of the eddy proportion on the diffusion coefficient is also controlled by different particle sizes. It can be seen from Fig. 18b that when the inlet flow velocity and arrangement mode (SC) are unchanged, the diffusion coefficient increases exponentially with the eddy proportion. And Fig. 18c show that the eddy proportion is proportional to the diffusion coefficient under the condition of different arrangement modes, it is found that the larger flow velocity will lead to larger the slope of the linear equation fitted by comparing two different flow velocities.

A key insight from this study is the confirmation that eddies act as dynamic regions of active solute retention and release, rather than as immobile water pockets. The measured non-zero velocities within the eddies (Fig. 6c) drive a continuous, albeit slower, exchange process with the main flow. This mechanism aligns with the modern understanding of vortex-driven anomalous dispersion, as detailed in studies like Bordoloi et al. (2022). Our findings, which establish a

quantitative link between eddy proportion, flow conditions, and the parameters of the MIM model, therefore build upon this paradigm by providing a pore-scale basis for upscaling the effects of such dynamic immobile zones in conceptual and numerical transport models.

In addition, the primary objective of this study is to investigate the basic physical mechanisms of eddy-driven non-Fickian transport by isolating key variables in a controlled system. This reductionist approach is a cornerstone of hydrological science, as it allows for the development of fundamental theories and parametric relationships that are often obscured in highly heterogeneous natural systems. The insights gained, specifically, the quantitative links between pore structure, eddy proportion, and the parameters of the Mobile-Immobile Model (MIM), which provided a mechanistic basis for understanding and predicting solute transport in more complex field scenarios. These include environments where similar processes dominate, such as in coarse-grained aquifer zones, fractured media, or engineered systems like filtration beds. By establishing these fundamental principles, our study provides the scientific basis and conceptual tools needed to improve the accuracy of models used for groundwater pollution prediction and remediation strategy optimization.

5 Summary and conclusion

The experimental and numerical simulation results of solute transport under three different control factors are presented in this study, and a quantitative characterization method for the eddy proportion on 3D scale is proposed. Besides, the generation, development and evolution of eddies with different factors in different porous media and their effects on solute transport are discussed. The main conclusions are as follows:

1. Different types of porous media structures (with varying particle sizes and arrangements) and inlet flow velocities determine the development and evolution of eddies, which in turn affects the solute transport process.
2. The exchange of solutes between the main flow stream and the eddy area is slowed down due to the lower flow velocity, resulting in solutes only entering the main flow stream through diffusion, which makes the tailing of the BTCs more pronounced. Smaller particle size will lead to a diminishing trend in the early breakthrough phenomenon of the solute. The penetration process of the BCC model is the fastest, followed by the FCC and SC models, while the penetration process of the RP model is the slowest.
3. The proportion of the immobile region inverted by the MIM model can be well matched with that of the eddy zone in porous media. Therefore, taking the eddy area proportion as the input term, on the one hand, endows

the parameters of the MIM model with clear physical meanings; On the other hand, taking the structural parameters of porous media as the basis for the inversion of MIM model parameters can optimize the multiple solutions and obtain more accurate model fitting results.

4. The mass transfer coefficient (α) and diffusion coefficient (D_{MIM}) of MIM model respond significantly to the different structure of porous media, and the D_{MIM} is proportional to the increase of inlet flow velocity, which is consistent with the results of different arrangement modes. And the D_{MIM} increases exponentially with the eddy proportion when the inlet flow velocity and arrangement mode (SC) are unchanged.

Code availability. The underlying software code can be made available by contacting the first author or the corresponding authors.

Data availability. The data can be made available by contacting the first author or the corresponding authors.

Author contributions. ZL: Writing-review & editing, Writing-original draft, Funding acquisition, Methodology, Conceptualization. XY: Data curation, Visualization. SY: Writing, Data analysis, Numerical simulation. JW: Data curation, Supervision. YY: Numerical simulation, Data curation. HF: Writing-review & editing, Methodology, Visualization. XK: Data analysis, Review & Editing. KH: Numerical simulation, Methodology, Visualization. CM: Methodology, Data analysis.

Competing interests. The contact author has declared that none of the authors has any competing interests.

Disclaimer. Publisher's note: Copernicus Publications remains neutral with regard to jurisdictional claims made in the text, published maps, institutional affiliations, or any other geographical representation in this paper. The authors bear the ultimate responsibility for providing appropriate place names. Views expressed in the text are those of the authors and do not necessarily reflect the views of the publisher.

Acknowledgements. This study was supported by the National Natural Science Foundation of China (Grant 42407085, 42272296), the Open Fund of Key Laboratory of Mine Ecological Effects and Systematic Restoration, Ministry of Natural Resources (No. MEER-2023-01), and the Natural Science Foundation of Hubei (No. 2025AFB139).

Financial support. This research has been supported by the National Natural Science Foundation of China (grant no. 42407085), the Open Fund of Key Laboratory of Mine Ecological Effects and

Systematic Restoration, Ministry of Natural Resources (grant no. MEER-2023-01), and the Natural Science Foundation of Hubei (grant no. 2025AFB139).

Review statement. This paper was edited by Xavier Sanchez-Vila and reviewed by two anonymous referees.

References

- Banaei, S., Javid, A., and Hassani, A.: Numerical simulation of groundwater contaminant transport in porous media, *Int. J. Environ. Sci. Te.*, 18, 151–162, <https://doi.org/10.1007/s13762-020-02825-7>, 2021.
- Bijeljic, B., Raeini, A., Mostaghimi, P., and Blunt, M. J.: Predictions of non-Fickian solute transport in different classes of porous media using direct simulation on pore-scale images, *Phys. Rev. E*, 87, 013011, <https://doi.org/10.1103/PhysRevE.87.013011>, 2013.
- Bordoloi, A. D., Scheidweiler, D., Dentz, M., Bouabdellaoui, M., Abbarchi, M., and de Anna, P.: Structure induced laminar vortices control anomalous dispersion in porous media, *Nat. Commun.*, 13, 3820, <https://doi.org/10.1038/s41467-022-31552-5>, 2022.
- Brusseau, M. L., Rao, P., and Gillham, R. W.: Sorption nonideality during organic contaminant transport in porous media, *Crit. Rev. Env. Sci. Tec.*, 19, 33–99, <https://doi.org/10.1080/10643388909388358>, 1989.
- Burri, N. M., Weatherl, R., Moeck, C., and Schirmer, M.: A review of threats to groundwater quality in the anthropocene, *Sci. Total Environ.*, 684, 136–154, <https://doi.org/10.1016/j.scitotenv.2019.05.236>, 2019.
- de Vries, E. T., Raouf, A., and van Genuchten, M. T.: Multiscale modelling of dual-porosity porous media; a computational pore-scale study for flow and solute transport, *Adv. Water Resour.*, 105, 82–95, <https://doi.org/10.1016/j.advwatres.2017.04.013>, 2017.
- Dou, Z., Chen, Z., Zhou, Z., Wang, J., and Huang, Y.: Influence of eddies on conservative solute transport through a 2D single self-affine fracture, *Int. J. Heat Mass Tran.*, 121, 597–606, <https://doi.org/10.1016/j.ijheatmasstransfer.2018.01.037>, 2018.
- Dou, Z., Sleep, B., Zhan, H., Zhou, Z., and Wang, J.: Multi-scale roughness influence on conservative solute transport in self-affine fractures, *Int. J. Heat Mass Tran.*, 133, 606–618, <https://doi.org/10.1016/j.ijheatmasstransfer.2018.12.141>, 2019.
- Gao, G., Zhan, H., Feng, S., Fu, B., Ma, Y., and Huang, G.: A new mobile-immobile model for reactive solute transport with scale-dependent dispersion, *Water Resour. Res.*, 46, W08533, <https://doi.org/10.1029/2009WR008707>, 2010.
- Gouze, P., Melean, Y., Le Borgne, T., Dentz, M., and Carrera, J.: Non-Fickian dispersion in porous media explained by heterogeneous microscale matrix diffusion, *Water Resour. Res.*, 44, W11416, <https://doi.org/10.1029/2007WR006690>, 2008.
- Harr, M. E.: *Groundwater and seepage*, Dover Publications, <https://www.perlego.com/book/111452/groundwater-and-seepage-pdf> (last access: 30 April 2026), 2012.
- Hasan, S., Joekar-Niasar, V., Karadimitriou, N. K., and Sahimi, M.: Saturation dependence of non-fickian transport in porous media, *Water Resour. Res.*, 55, 1153–1166, <https://doi.org/10.1029/2018WR023554>, 2019.
- Hou, Y., Jiang, J., and Wu, J.: Anomalous Solute Transport in Cemented Porous Media: Pore-scale Simulations, *Soil Sci. Soc. Am. J.*, 82, 10–19, <https://doi.org/10.2136/sssaj2017.04.0125>, 2018.
- Huang, K., Wan, J., Chen, C., Linqing, H., Mei, W., and Zhang, M.: Experimental investigation on water flow in cubic arrays of spheres, *J. Hydrol.*, 492, 61–68, <https://doi.org/10.1016/J.JHYDROL.2013.03.039>, 2013.
- Karadimitriou, N. K., Joekar-Niasar, V., Babaei, M., and Shore, C. A.: Critical role of the immobile zone in non-Fickian two-phase transport: a new paradigm, *Environ. Sci. Technol.*, 50, 4384–4392, <https://doi.org/10.1021/acs.est.5b05947>, 2016.
- Kitanidis, P. K.: The concept of the dilution index, *Water Resour. Res.*, 30, 2011–2026, <https://doi.org/10.1029/94WR00762>, 1994.
- Kohne, J. M., Kohne, S., Mohanty, B. P., and Šimunek, J.: Inverse mobile-immobile modeling of transport during transient flow: Effects of between-domain transfer and initial water content, *Vadose Zone J.*, 3, 1309–1321, <https://doi.org/10.2136/vzj2004.1309>, 2004.
- Koohbor, B., Colombano, S., Harrouet, T., Deparis, J., Lion, F., Davarzani, D., and Ataie-Ashtiani, B.: The effects of water table fluctuation on LNAPL deposit in highly permeable porous media: A coupled numerical and experimental study, *J. Contam. Hydrol.*, 256, 104183, <https://doi.org/10.1016/j.jconhyd.2023.104183>, 2023.
- Lee, J. and Babadagli, T.: Effect of roughness on fluid flow and solute transport in a single fracture: A review of recent developments, current trends, and future research, *J. Nat. Gas Sci. Eng.*, 91, 103971, <https://doi.org/10.1016/j.jngse.2021.103971>, 2021.
- Li, Y., Chen, L., and Shi, Y.: Influence of 3D Fracture Geometry on Water Flow and Solute Transport in Dual-Conduit Fracture, *Water*, 15, 1754, <https://doi.org/10.3390/w15091754>, 2023.
- Li, Z., Yang, Y., Zhan, H., Wan, J., Cheng, J., Feng, H., and Yang, X.: On the advection–diffusion process with developing eddies in karst conduits, *Geophys. Res. Lett.*, 51, e2024GL111214, <https://doi.org/10.1029/2024GL111214>, 2024.
- Llamas, M. R. and Martínez-Santos, P.: Intensive groundwater use: silent revolution and potential source of social conflicts, *J. Water Res. Plan. Man.*, 131, 337–341, [https://doi.org/10.1061/\(ASCE\)0733-9496\(2005\)131:5\(337\)](https://doi.org/10.1061/(ASCE)0733-9496(2005)131:5(337)), 2005.
- Polubarinova-Kochina, P. Y., Wiest, R. D., and Wiest, R. D.: *Theory of Ground Water Movement*, Princeton University Press, <https://www.perlego.com/book/739067/theory-of-ground-water-movement-pdf> (last access: 29 April 2026), 2015.
- Shah, T., Roy, A. D., Qureshi, A. S., and Wang, J.: Sustaining Asia’s groundwater boom: an overview of issues and evidence, *Nat. Resour. Forum*, 130–141, <https://doi.org/10.1111/1477-8947.00048>, 2003.
- Šimunek, J., He, C., Pang, L., and Bradford, S.: Colloid-facilitated solute transport in variably saturated porous media: Numerical model and experimental verification, *Vadose Zone J.*, 5, 1035–1047, <https://doi.org/10.2136/vzj2005.0151>, 2006.
- Tang, D., Frind, E., and Sudicky, E. A.: Contaminant transport in fractured porous media: Analytical solution for

- a single fracture, *Water Resour. Res.*, 17, 555–564, <https://doi.org/10.1029/WR017i003p00555>, 1981.
- Vaughan, P.: Assumption, prediction and reality in geotechnical engineering, in: *Selected papers on geotechnical engineering* by PR Vaughan, Thomas Telford Publishing, 305–341, <https://doi.org/10.1680/geot.1994.44.4.573>, 2009.
- Wang, Z.: Seepage in Soils—Principles and Applications, *Vadose Zone J.*, 3, 728–729, <https://doi.org/10.2136/vzj2004.0728>, 2004.
- Xiong, T., Li, Z., Zhan, H., Wan, J., Huang, K., Yuan, S., and Xiao, J.: Two-dimensional high-resolution numerical investigation of eddy effect in artificial rough conduits with different shapes, *Adv. Water Resour.*, 184, 104621, <https://doi.org/10.1016/j.advwatres.2024.104621>, 2024.
- Yang, X., Ji, Z., Zhang, P., and Qi, J.: Model test and numerical simulation on the development of artificially freezing wall in sandy layers considering water seepage, *Transportation Geotechnics*, 21, 100293, <https://doi.org/10.1016/j.trgeo.2019.100293>, 2019.
- Yu, P., Wang, D., Wan, C., Liu, J., Li, Y., Munir, B., and Du, D.: A pore-scale numerical study on the seepage characteristics in low-permeable porous media, *Environ. Earth Sci.*, 82, 268, <https://doi.org/10.1007/s12665-023-10953-9>, 2023.
- Zheng, L., Wang, L., Wang, T., Wang, Z.-L., and Chen, X.: Mass transfer between recirculation zone and main flow domain in fractures: Is the first order rate law valid?, *J. Hydrol.*, 613, 128352, <https://doi.org/10.1016/j.jhydrol.2022.128352>, 2022.
- Zhou, J. Q., Wang, L., Chen, Y. F., and Cardenas, M. B.: Mass transfer between recirculation and main flow zones: Is physically based parameterization possible?, *Water Resour. Res.*, 55, 345–362, <https://doi.org/10.1029/2018WR023124>, 2019.